INTERFACE

rsif.royalsocietypublishing.org

Research

Cite this article: Li J *et al*. 2016 Controlled cobalt doping in the spinel structure of magnetosome magnetite: new evidences from element- and site-specific X-ray magnetic circular dichroism analyses. *J. R. Soc. Interface* **13**: 20160355.
http://dx.doi.org/10.1098/rsif.2016.0355

Received: 4 May 2016
Accepted: 14 July 2016

Subject Category:
Life Sciences–Physics interface

Subject Areas:
biomaterials, nanotechnology, biomimetics

Keywords:
magnetotactic bacteria, biomineralization, cobalt-doped magnetite, X-ray magnetic circular dichroism, coordination chemistry, magnetic alteration

Author for correspondence:
Jinhua Li
e-mail: lijinhua@mail.iggcas.ac.cn

Electronic supplementary material is available at http://dx.doi.org/10.1098/rsif.2016.0355 or via http://rsif.royalsocietypublishing.org.

THE ROYAL SOCIETY PUBLISHING

Controlled cobalt doping in the spinel structure of magnetosome magnetite: new evidences from element- and site-specific X-ray magnetic circular dichroism analyses

Jinhua Li[1,2], Nicolas Menguy[2,3], Marie-Anne Arrio[3], Philippe Sainctavit[3,4], Amélie Juhin[3], Yinzhao Wang[1,2], Haitao Chen[5], Oana Bunau[3], Edwige Otero[4], Philippe Ohresser[4] and Yongxin Pan[1,2]

[1]Paleomagnetism and Geochronology Laboratory, Key Laboratory of Earth and Planetary Physics, Institute of Geology and Geophysics, and [2]France-China Biomineralization and Nano-structures Laboratory, Chinese Academy of Sciences, Beijing 100029, People's Republic of China
[3]IMPMC, CNRS UMR 7590, Sorbonne Universités, MNHN, UPMC, IRD UMR 206, 75005 Paris, France
[4]Synchrotron SOLEIL, L'Orme des Merisiers Saint-Aubin, 91192 Gif-Sur-Yvette Cedex, France
[5]Institute of Deep-Sea Science and Engineering, Chinese Academy of Sciences, Sanya 572000, People's Republic of China

JL, 0000-0003-1622-6170

The biomineralization of magnetite nanocrystals (called magnetosomes) by magnetotactic bacteria (MTB) has attracted intense interest in biology, geology and materials science due to the precise morphology of the particles, the chain-like assembly and their unique magnetic properties. Great efforts have been recently made in producing transition metal-doped magnetosomes with modified magnetic properties for a range of applications. Despite some successful outcomes, the coordination chemistry and magnetism of such metal-doped magnetosomes still remain largely unknown. Here, we present new evidences from X-ray magnetic circular dichroism (XMCD) for element- and site-specific magnetic analyses that cobalt is incorporated in the spinel structure of the magnetosomes within *Magnetospirillum magneticum* AMB-1 through the replacement of Fe^{2+} ions by Co^{2+} ions in octahedral (O_h) sites of magnetite. Both XMCD at Fe and Co $L_{2,3}$ edges, and energy-dispersive X-ray spectroscopy on transmission electron microscopy analyses reveal a heterogeneous distribution of cobalt occurring either in different particles or inside individual particles. Compared with non-doped one, cobalt-doped magnetosome sample has lower Verwey transition temperature and larger magnetic coercivity, related to the amount of doped cobalt. This study also demonstrates that the addition of trace cobalt in the growth medium can significantly improve both the cell growth and the magnetosome formation within *M. magneticum* AMB-1. Together with the cobalt occupancy within the spinel structure of magnetosomes, this study indicates that MTB may provide a promising biomimetic system for producing chains of metal-doped single-domain magnetite with an appropriate tuning of the magnetic properties for technological and biomedical applications.

1. Introduction

Magnetic nanoparticles (MNPs) have a broad range of applications from data storage to medical imaging and to hyperthermia treatment of tumours [1–3]. Tailored synthesis of MNPs by which the physical and magnetic properties are well controlled is essential for determining the technological and biomedical

applications that they are suitable for. For instance, MNPs with single-domain (SD) sizes and one-dimensional (1D) arrays have advantages in magnetic memory devices [4] and magnetic hyperthermia [5] due to their stronger magnetic anisotropy and hysteresis than their random assemblages [6–8].

A number of methods including co-precipitation, hydrothermal approaches and mechanical ball milling have been developed to produce nanocrystals of magnetite (Fe_3O_4) or maghemite (γ-Fe_2O_3), the most popular MNPs in biomedical applications due to their low toxicity and high magnetization, for different commercial uses [9]. However, these methods often involve high temperature with toxic solvents resulting in high environmental and energy costs. Recently, synthesis of MNPs by biotic processes such as microbial biomineralization [10–16] or biocatalysis by biomolecules [17–23] has attracted a great interest in producing novel MNPs with high quality and biocompatibility under environment friendly conditions (e.g. at room temperature and ambient pressure and in toxic-free solutions).

Magnetotactic bacteria (MTB) have an incredible ability to form nanocrystals of SD magnetite within intracellular lipid vesicles (named as magnetosomes) that have high chemical purity, narrow size and shape distributions, species- or strain-specific crystal morphologies, and are usually organized into chain(s) [24–26]. By using the magnetosome chain(s), MTB cells orient themselves and navigate along the Earth's magnetic field lines when they are swimming in aquatic environments [24]. As an intriguing model system, MTB have, therefore, been extensively studied for better understanding the magnetite biomineralization and geomagnetic sensitivity in organisms [24,25], but also have recently been modified for producing physically and biologically tailored MNPs [13,27,28]. For instance, to enhance the magnetic hardness of magnetosome magnetite, Staniland *et al*. [13] pioneered a cobalt-doping study of magnetosomes within three cultured strains of the bacterium *Magnetospirillum*. They have shown that the presence of cobalt increases the coercivity of the magnetosomes by 36–45%, depending on the bacterial strains and the cobalt contents. Recently, Tanaka *et al*. [11] further increased the levels of cobalt doping approximately up to 3.0% by increasing the concentration of cobalt ions in the initial culture medium. It has been evidenced that the presence of cobalt in the magnetosomes significantly increases the magneto-crystalline anisotropy constant and the magnetic hysteresis, and therefore increases the heating efficiency for applications in alternating magnetic field cancer therapy [29]. These previous studies are extremely important for the development of functionalized magnetosomes for biotechnological and biomedical applications. However, one fundamental question, i.e. the coordination chemistry and magnetism of cobalt within the magnetosomes, still remains largely unknown, and information on the structure and the magnetic properties of Co-doped magnetosomes is very limited.

In this study, we investigate the magnetosome formation in *Magnetospirillum magneticum* AMB-1 anaerobically grown under three $[Co^{2+}]/[Fe^{3+}]$ ratio conditions: 0/22.1 μM, 2.1/20 μM and 12.1/10 μM, hereafter referred to as Co(0), Co(2.1) and Co(12.1), respectively. Scanning transmission electron microscopy (STEM) observations show that the presence of trace cobalt in the initial growth medium (e.g. 2.1 μM) significantly improved the cell growth and magnetosome formation. Rock magnetic measurements on the whole-cell samples reveal that, compared with the Co(0) magnetosomes, the Co(2.1) and Co(12.1) magnetosomes have reduced Verwey transition temperature (T_v) and increased coercivity (B_c) values, e.g. $T_v = 108$ K, $B_c(300\ K) = 14.4$ mT and $B_c(5\ K) = 74.0$ mT for the Co(0) versus $T_v = 100$ K, $B_c(300\ K) = 27.3$ mT and $B_c(5\ K) = 275.4$ mT for the Co(12.1). The site occupancy, valence and distribution of cobalt within the magnetosomes have further been studied by X-ray absorption spectroscopy (XAS) and X-ray magnetic circular dichroism (XMCD) at both Fe and Co $L_{2,3}$ edges. Experimental and theoretical XMCD analyses reveal a heterogeneous distribution of cobalt occurring either in different particles or inside individual particles. Within cobalt-doped magnetosomes, only Co^{2+} was incorporated in octahedral (O_h) sites of magnetite through the substitution of Fe^{2+}. These findings are supported by energy-dispersive X-ray spectroscopy (EDXS) performed by transmission electron microscopy (TEM) on individual particles. Finally, the potential process of cobalt doping in the magnetosomes and its significance in the tailored synthesis of MNPs are discussed.

2. Experimental

2.1. Bacterial growth and sample preparation

Magnetospirillum magneticum strain AMB-1 (ATCC74205) was used in this study, and the cells were grown within a modified ATCC-recommended medium where $CoCl_2$ was omitted from the Wolf's mineral solution, and cobalt and iron sources were added in three different proportions: 22.1 μM of Fe^{3+}-quinate, 2.1 μM of Co^{2+}-quinate plus 20 μM of Fe^{3+}-quinate or 12.1 μM of Co^{2+}-quinate plus 10 μM of Fe^{3+}-quinate. These three cultures were hereafter termed as Co(0), Co(2.1) and Co(12.1), respectively. The Co(2.1) culture actually contains same concentration of Co^{2+} to the normal ATCC-recommended medium, where Co^{2+} was supplied by $CoCl_2$ through the Wolf's mineral solution. The cell cultures were performed anaerobically in a YQX-II anaerobic incubator (ShangHai CIMO Medical Instrument Co. Ltd, $[O_2] < 300$ pm) at 26°C [30]. For each culture, 2.5 l of cells were grown. After grown to the stationary phase (i.e. 96 h), all bacterial cultures were harvested by centrifugation at 8000 r.p.m. at 4°C for 10 min and immediately stored at −20°C under nitrogen protection for further processing.

About 10^{10} cells were loaded into a non-magnetic gelatin capsule and dried at ambient temperature within a COY anaerobic chamber (COY Labs, USA, $[O_2] < 100$ ppm) overnight for magnetic measurements. Other cells were used for isolating magnetosomes for X-ray absorption and magnetic circular dichroism measurements. To do this, the cells were resuspended into approximately 100 ml of Milli-Q water, disrupted by an ultrasonicator (VCX 130, SONICS, USA); magnetosomes were magnetically collected with a bar magnet and then washed with distilled water at least five times. To avoid possible post-oxidization of magnetosomes during the extraction, the whole process of cell disruption and magnetosome isolation was performed inside the COY anaerobic chamber as described in Li *et al*. [31]. Milli-Q water was heated to 80°C and degassed by bubbling with nitrogen for 1 h to remove dissolved oxygen. The extracted magnetosomes were stored in 0.2 ml of degassed 100% alcohol in a 2 ml Crimp-Top vial (Sigma-Aldrich). All the whole-cell and isolated magnetosome samples were maintained in pure nitrogen atmosphere at −20°C prior to measurements.

2.2. Transmission electron microscopy analyses

For TEM analyses, intact cells or extracted magnetosomes of AMB-1 were deposited onto carbon-coated copper grids and studied with a JEOL 2100F microscope operating at 200 kV. This microscope was equipped with a field emission gun, a high-resolution UHR pole piece and a JEOL detector with an ultrathin window allowing detection of light elements, and a STEM device, which allows *Z*-contrast imaging in high-angle annular dark field (HAADF) mode. Magnetosome numbers and sizes were analysed using standard analytical software for processing digitized HAADF-STEM images (IMAGE J). The dimensions were estimated by determining the best fit of an ellipse to the projection of the particle. The major and minor axes of the best fitting ellipse were used as the length (L) and width (W) of the crystal, respectively. The grain size was defined as $(L + W)/2$, and the shape factor as W/L. Here we used HAADF-STEM imaging rather than conventional bright-field TEM, because the former is also efficient enough for imaging those very small magnetosomes (less than 5 nm) due to their big chemical contrast from surrounding cytoplasm. Therefore, the combination of HAADF-STEM imaging and ellipse fitting is believed to produce negligible artefacts in the size distributions [32].

2.3. Rock magnetic measurements

Room-temperature, first-order reversal curves (FORCs) were measured using a VSM3900 magnetometer (Princeton Measurements Corporation VSA 3900, sensitivity $= 5.0 \times 10^{10}$ Am^2) following the protocol as described by Roberts *et al*. [33]. For each sample, a total 120 curves were measured with a positive saturation field of 500 mT, an increasing field step (δ) of 1.87 mT and an average time of 200 ms. The FORC diagrams were calculated using the FORCINEL version 2.05 software with a smooth factor of 3 [34], and the FORC characteristic coercivity ($B_{c,FORC}$) was given by the median coercivity of the marginal coercivity distribution [6].

Low-temperature magnetic measurements were performed with a Quantum Design MPMS XP-5 SQUID magnetometer (sensitivity $= 5.0 \times 10^{10}$ Am^2). Thermal demagnetization curves were obtained by cooling samples from 300 to 10 K in zero field (ZFC) and in a 2.5 T field (FC), respectively, followed by imparting a saturation isothermal remanent magnetization (SIRM) in a 2.5 T field (hereafter termed as $SIRM_{10K\_2.5T}$), and then measuring the remanence in zero field during warming up to 300 K. The Verwey transition temperature (T_v) of magnetite was defined as the temperature of the maximum of the first derivative of the FC curves, and the Verwey transition signature of magnetosome chains is characterized by the δ-ratio (δ_{FC}/δ_{ZFC}), in which δ_{FC} and δ_{ZFC} are calculated as $\delta = (M_{80K} - M_{150K})/M_{80K}$, where M_{80K} and M_{150K} are the remanences measured at 80 K and 150 K, respectively [35].

Low-temperature hysteresis loops between ± 3 T and backfield SIRM demagnetization curves were measured also with the MPMS XP-5 SQUID magnetometer, and the corresponding magnetic hysteresis parameters including coercivity (B_c), saturation magnetization (M_s) and saturation remanence (M_{rs}) were determined after applying the high-field (1–3 T) slope corrections for linear contributions from the paramagnetic phase. Remanence coercivity (B_{cr}) was determined from the backfield SIRM demagnetization curve.

2.4. X-ray absorption and magnetic circular dichroism measurements

XAS and XMCD spectra at Fe and Co $L_{2,3}$ edges were obtained on beamline DEIMOS at the French synchrotron radiation source SOLEIL (Proposal number: 20110175). The DEIMOS beamline has been optimized for stability and reproducibility in terms of photon flux and photon energy. The main end-station consists in a cryo-magnet with two split coils providing a 7 T magnetic field along the beam or 2 T perpendicular to the beam with a controllable temperature on the sample from 370 K down to 1.5 K. It delivers polarized soft X-rays to perform XAS, XMCD and X-ray linear dichroism in the energy range from 350 to 2500 eV [36]. A glove box is also available in the DEIMOS beamline which allows the whole process of sample preparation and insertion into the beamline under oxygen-free environments. Inside such beamline-connected anaerobic cabinet, the extracted magnetosomes were mounted on acetone-washed silicon wafer surface attached to the sample manipulator. After being anaerobically dried within the glove box, samples were loaded by saturating the manipulator in a stream of nitrogen gas during insertion into the vacuum chamber. The specimen was positioned central to the magnetic pole pieces, with the X-ray beam entering through a small centred hole in one of the pole pieces, parallel to the magnetic field and perpendicular to the sample surface. The incoming photon flux and the absorbed photon flux were monitored in total electron yield mode, which gives an effective probing depth of approximately 5 nm.

The XMCD signals were recorded by both flipping the circular polarization (either left or right helicity) and the external magnetic field. The XMCD signal was obtained as the difference $t_{XMCD} = \sigma^- - \sigma^+$, where $\sigma^- = [\sigma_L(B^-) + \sigma_R(B^+)]/2$, $\sigma^- = [\sigma_L(B^+) + \sigma_R(B^-)]/2$, σ_L (σ_R) is the cross-section with left (right) polarized X-rays, and B^+ (B^-) the magnetic field parallel (antiparallel) to the X-ray propagation vector. This procedure ensured a high signal-to-noise ratio and allowed us to discard any spurious systematic signals. In this study, all the XAS spectra have been measured for samples cooled to 4 K and in an external magnetic field of 0.6 T.

We have also measured element-specific magnetization curves detected by XMCD at 3 K. This has been done by setting the energy of monochromator at the energy where the XMCD signal is maximized (in absolute value) and then switching the magnetic field between ± 0.6 T on the fly while collecting the total electron yield of the sample.

2.5. X-ray absorption spectroscopy and X-ray magnetic circular dichroism data processing

We performed a quantitative analysis of the Co(0) and Co(12.1) XAS and XMCD spectra by fitting the data with the XAS and XMCD experimental spectra of maghemite and magnetite with accurate known stoichiometry [37,38]. The robustness of the method was first tested by reproducing very accurately the XAS and XMCD signals for the Co(0) sample. It was then applied to the Co(12.1) sample, and the missing fraction of Fe^{2+} in O_h sites allowed the determination of the Co^{2+} content in O_h sites.

XAS and XMCD spectra were simulated at the Co $L_{2,3}$ edges using ligand field multiple calculations developed by Thole *et al*. [39]. The details can be found in

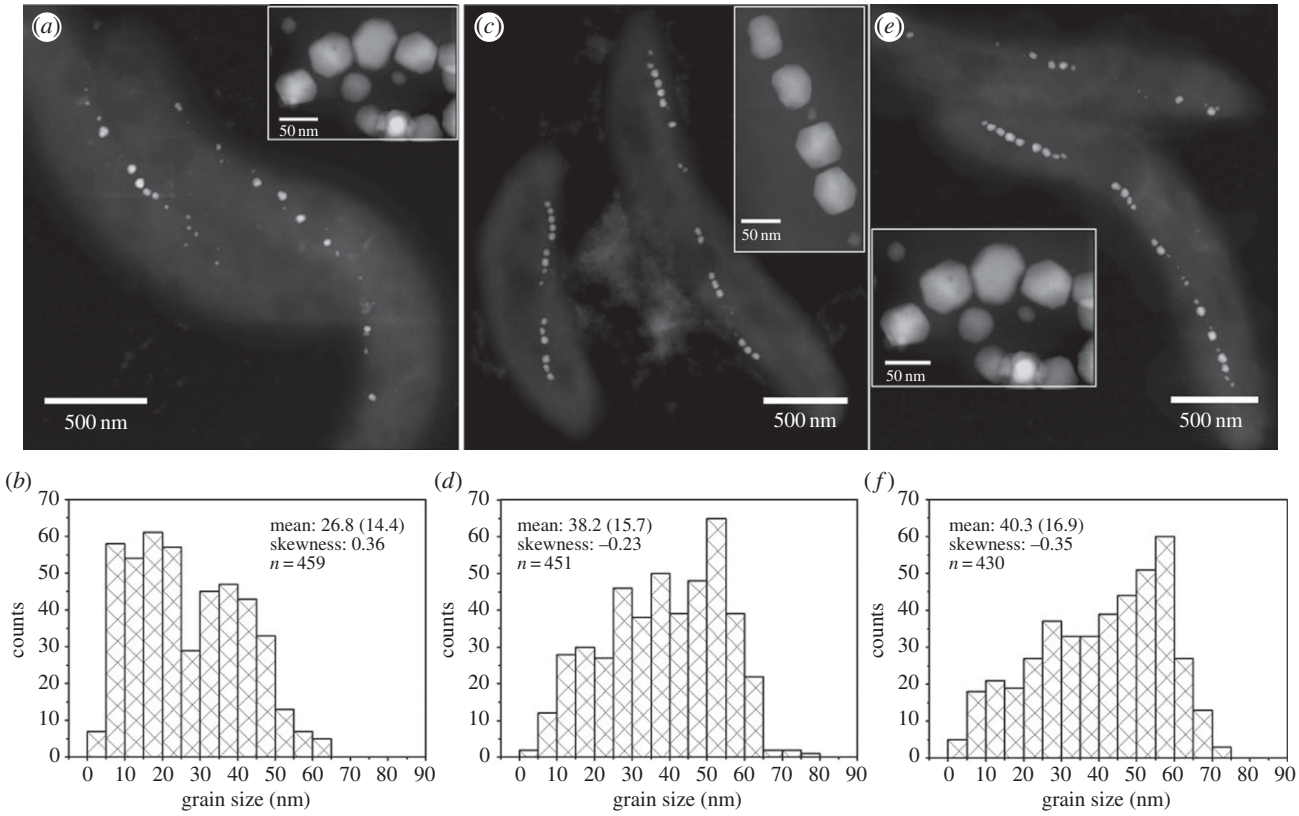

Figure 1. Characterization of magnetosomes produced by AMB-1 cells within the Co(0) (*a*,*b*), Co(2.1) (*c*,*d*) and Co(12.1) (*e*,*f*) cultures. (*a*,*c*,*e*) HAADF-STEM images of AMB-1 cells and magnetosomes, while (*b*,*d*,*f*) indicate the corresponding grain size distributions (values of mean size (standard deviation), distribution skewness and statistics number are shown in each panel).

Arrio *et al*. [40]. The calculations for the simulation of the Co $L_{2,3}$ edges have been performed in an octahedral environment with the spin orbit coupling acting on the 3d shell, $\zeta_{3d} = 22$ meV, the reduction of the Slater integrals $\kappa = 70\%$, the cubic crystal field parameter 10Dq = 1 eV, a HWHM broadening by a Lorentzian function $\Gamma_{L3} = 0.2$ eV at the L_3 edge and $\Gamma_{L2} = 0.4$ at the L_2 edge and a HWHM broadening by a Gaussian function $\sigma = 0.1$ eV K

3. Results

3.1. Magnetosome number, grain size and chain arrangement

STEM observations at HAADF mode reveal that the presence of cobalt in the initial growth medium significantly improved the magnetosome formation and chain organization, i.e. more magnetosomes with larger sizes and longer chains were produced in the Co(2.1) and Co(12.1) cultures than in the Co(0) culture (figure 1; electronic supplementary material, figure S1). In the Co(0) culture, the AMB-1 cells synthesized 17 magnetosomes on average, with a mean size of 26.8 ± 14.4 nm and shape factor of 0.84 ± 0.11. These values increase to 21 magnetosomes, and 38.2 ± 15.7 nm and 0.83 ± 0.09 for the Co(2.1) culture, and 19 magnetosomes, and 40.3 ± 16.9 nm and 0.80 ± 0.09 for the Co(12.1) culture, respectively. The grain size distributions of magnetosomes produced within the Co(2.1) and Co(12.1) cultures are characterized by negatively skewed shapes with the skewness value of −0.23 and −0.35, respectively. In contrast, the magnetosomes produced in the Co(0) culture have a positive skew distribution with the skewness value of 0.36. This indicates that most magnetosomes are close to their mature sizes within the Co(2.1) and Co(12.1) cultures, while they are immature within the Co(0) culture [41]. Notably, there were no obvious differences in the crystal morphology and the number of twinned crystals among these three cultures. Since all the three cultures were performed under the same total cation concentration of $[Co^{2+}] + [Fe^{3+}]$, the differences in the magnetosome formation (i.e. numbers, grain sizes and chain configurations) among them should be ascribed to the presence and content of cobalt rather than to the deficiency of cation source.

3.2. Magnetic properties

All the three samples have FORC diagrams that similarly present a set of closed contours with narrow vertical distribution around a specific coercivity value (figure 2*a*,*d*,*g*), indicating that dominantly SD magnetosomes were formed within AMB-1 cells under these three culture conditions [41]. With the increase of $[Co^{2+}]$ in the initial growth medium, the horizontal FORC distribution shifting towards the right clearly shows an increase of coercivity for magnetosomes produced within the presence of cobalt [41]. Specifically, the characteristic coercivity determined by the FORC ($B_{c,FORC}$) increases from approximately 30.5 mT for the Co(0) culture to approximately 38.6 mT for the Co(2.1), and to approximately 40.7 mT for the Co(12.1) at room temperature. The increase in the coercivity could be interpreted as either the increase in grain size and chain integrity or cobalt doping within the magnetosomes, or both, as reported previously by Staniland *et al*. [13].

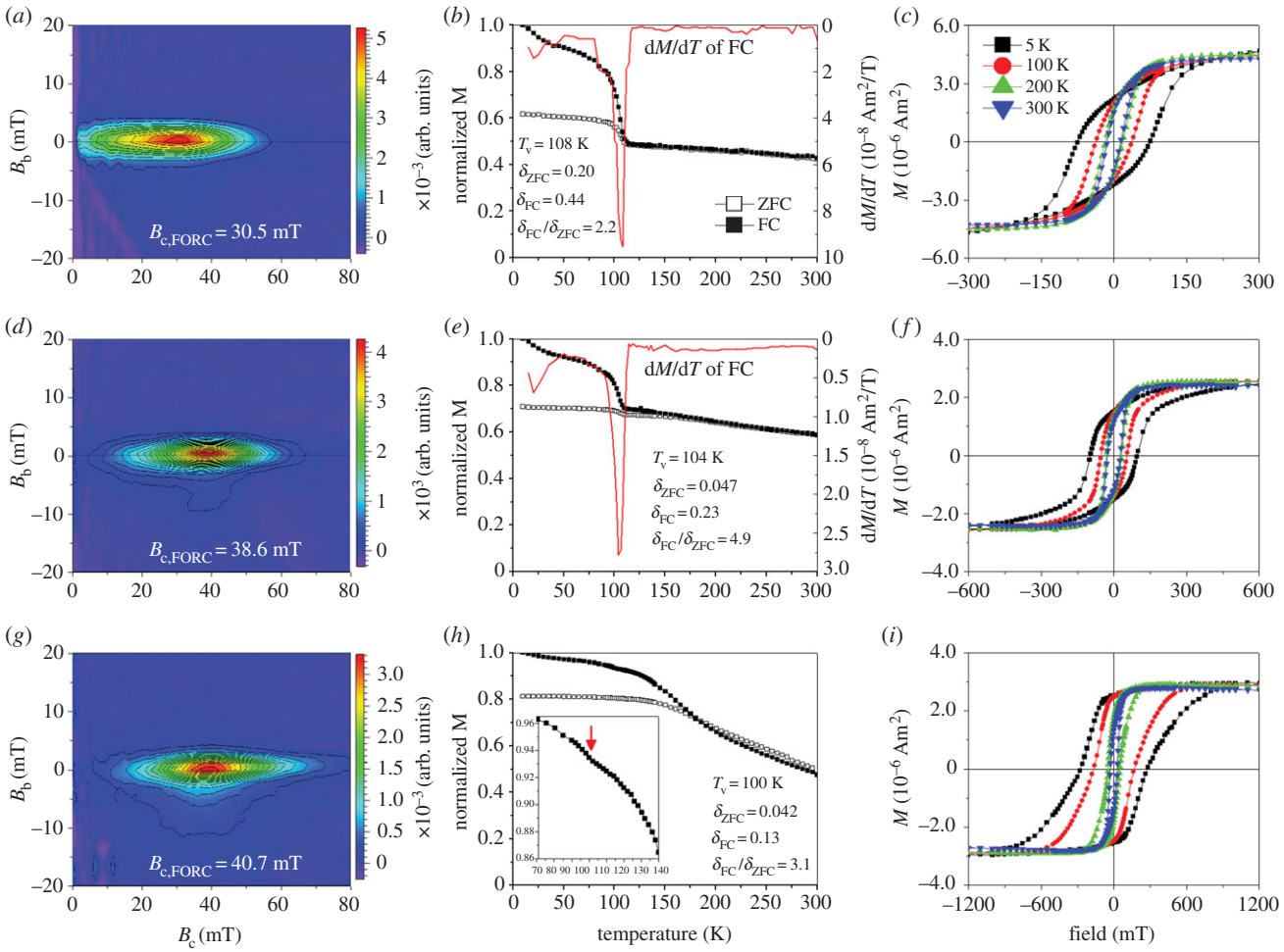

Figure 2. Magnetic properties of magnetosomes produced by AMB-1 cells within the Co(0) (*a*–*c*), Co(2.1) (*d*–*f*) and Co(12.1) (*g*–*i*) cultures. (*a*,*d*,*g*) Room-temperature, first-order reversal curves (FORCs) diagrams; (*b*,*e*,*h*) thermal decays of saturation remanence magnetization imparted at 2.5 T at 10 K after cooling the sample from 300 to 10 K in a 2.5 T field (FC) and zero field (ZFC); (*c*,*f*,*i*) hysteresis loop measured at temperatures 5, 100, 200 and 300 K. Note that the *x*-axes scales of (*c*), (*f*) and (*i*) are different.

To test whether the magnetic changes result from the chemical alteration of magnetosome crystals, we measured thermal demagnetization curves from 10 to 300 K and magnetic hysteresis loops at different low temperatures. As shown in figure 2*b*, the abrupt decrease in remanence around 100–110 K on the thermal decays of saturation remanence magnetization acquired at 2.5 T field at 10 K ($SIRM_{2.5T\_10K}$) after cooling in a field of 2.5 T (FC) or zero (ZFC) indicates the Verwey transition of magnetosome magnetite, as observed in previous studies [41]. The difference between the remanence losses of FC (δ_{FC}) and ZFC (δ_{ZFC}) curves upon warming across the Verwey transition, quantitatively described as δ_{FC}/δ_{ZFC}, is related to the chain configuration of magnetosomes [31,35,41]. As expected, the Verwey transition behaviours of the magnetosomes are distinctly different among the three cultures (figure 2*b*,*e*,*h*). Importantly, unlike the sharp transition observed in both FC and ZFC curves for the Co(0) sample, the Verwey transition signals of the Co(2.1) and Co(12.1) samples are suppressed, and only a small drop can be observed at approximately 100 K on FC curve of the Co(12.1) (see the inset in figure 2*h*). Since the three cultures dominantly produce SD magnetosomes with similar crystal morphology and frequency of twinned crystals, the observed decrease of δ_{FC} and δ_{ZFC}, and increase of δ_{FC}/δ_{ZFC} with the increase of $[Co^{2+}]$ in the initial growth medium can be interpreted as an enhancement of the shape anisotropy of magnetosome chain [31,35,41], resulting from longer chains of magnetosomes within the Co(2.1) and Co(12.1) cultures compared with the Co(0) culture, as observed by TEM (figure 1). In addition, the observed decrease of T_v, from 108 K for the Co(0), to 104 K for the Co(2.1) and to approximately 100 K for the Co(12.1), strongly indicates an overall decrease of magnetite purity or increase of crystalline disorder, or both, for magnetosomes as can be expected if cobalt ions enter the Fe_3O_4 spinel structure [42].

Consistently, the magnetic hysteresis differs significantly among the three cultures (figure 2*c*,*f*,*i*). Both coercivity (B_c) and remanence coercivity (B_{cr}) measured at each same temperature enlarge with the increase of $[Co^{2+}]$ within the initial growth medium (table 1). With the measuring temperature decreasing from 300 to 5 K, the differences in B_c and B_{cr} between the Co(0) and Co(12.1) cultures become larger and larger, while they become smaller and smaller between the Co(0) and Co(2.1) cultures (table 1). For instance, B_c and B_{cr} at 300 K are 14.4 mT and 25.8 mT, respectively, for the Co(0) sample, 27.0 mT and 34.3 mT, respectively, for the Co(2.1) sample, and 27.3 mT and 36.9 mT, respectively, for the Co(12.1) sample, while at 5 K they become 74.0 mT (B_c) and 99.4 mT (B_{cr}) for the Co(0) sample, 97.4 mT and 117.4 mT for the Co(2.1) culture, and 275.5 mT (B_c) and 314.5 mT (B_{cr}) for the Co(12.1) culture. Since more and more small magnetosomes become magnetically blocked with

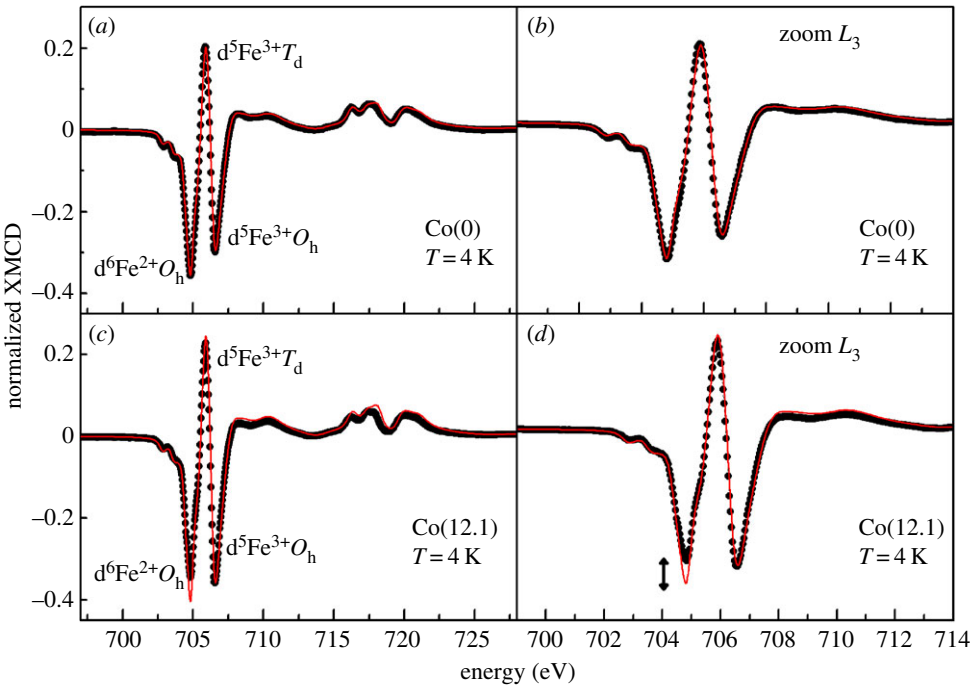

Figure 3. XMCD spectra measured at Fe $L_{2,3}$ edges on the Co(0) magnetosomes (*a*,*b*) and on the Co(12.1) magnetosomes (*c*,*d*). The experimental XMCD signals are plotted in black dots and compared with the result of the best linear combination (red line) of maghemite and magnetite reference samples (see Methods). The arrow in (*d*) indicates the missing fraction of Fe^{2+} in O_h site that is interpreted as resulting from Co^{2+} substitution.

Table 1. Summary of the physical properties of magnetosomes produced by AMB-1 in three different cultures.

				B_c/B_{cr} (mT)							
sample	size (nm)	T_v (K)	δ-ratio	300 K	250 K	200 K	150 K	100 K	50 K	10 K	5 K
Co(0)	26.8 ± 13.4	108	2.2	14.4/25.8	16.9/29.1	17.8/31.5	18.5/31.7	37.4/54.4	59.9/79.9	72.3/96.5	74.0/99.4
Co(2.1)	38.2 ± 15.7	104	4.9	27.0/34.3	28.4/37.2	31.5/40.7	32.9/43.8	52.5/67.8	77.3/95.0	93.8/112.7	97.4/117.4
Co(12.1)	40.3 ± 16.9	100	3.1	27.3/36.9	32.7/48.7	49.0/71.4	87.9/108.0	168.1/185.8	233.0/256.6	274.3/308.6	275.5/314.5

temperature decreasing from 300 to 5 K and start to contribute to the observed magnetic hysteresis, the effect of grain size distribution on B_c and B_{cr} becomes smaller and even negligible at 5 K [43]. Therefore, a nearly fourfold rise in the B_c and B_{cr} values at 5 K for the Co(12.1) culture to the Co(0) culture should result from chemical changes in the magnetosomes, i.e. cobalt was doped in the magnetosomes within the Co(12.1) culture. While, despite similar magnetic hysteresis at 300 K, a nearly twofold rise in the B_c and B_{cr} values at 5 K for the Co(12.1) culture compared with the Co(2.1) culture might indicate that the cobalt content in the Co(2.1) doped magnetosomes could be tiny.

In addition, compared with the pot-bellied shape for the Co(0) and Co(2.1) samples (figure 2*c*,*f*), the hysteresis loop for the Co(12.1) becomes wasp-waisted when measured at 100 and 5 K (figure 2*i*). Generally, a wasp-waisted hysteresis indicates a range of grain sizes, mixed magnetic mineralogy and/or a mixture of grains with heterogeneous composition [44]. In our case, only spinels with narrow grain size distribution were produced by the AMB-1 cells within the three cultures, as observed by TEM. Therefore, the wasp-waisted hysteresis particularly observed at low temperatures only for the Co(12.1) magnetosomes may suggest a heterogeneous doping of cobalt within individual particles.

3.3. Coordination chemistry of cobalt within the magnetosome magnetite

To determine the coordination chemistry of cobalt within the spinel structure of magnetosomes, both XAS and XMCD at Fe and Co $L_{2,3}$ edges were performed on the magnetosomes produced within the Co(0) and Co(12.1) cultures. The experimental XMCD spectra at Fe $L_{2,3}$ edges were fitted by a linear combination of experimental XMCD signal for pure magnetite and pure maghemite (electronic supplementary material, figure S2) [37,38]. As shown in figure 3, the composition of the magnetosomes produced by the AMB-1 cells in the Co(0) culture slightly deviates from stoichiometric magnetite, which possibly results from crystal defects (e.g. cation vacancy) occurring during magnetosome biomineralization [30]. From the linear combination of the fit in figure 3, one can determine that the calculated ratio of $Fe^{2+}O_h : Fe^{3+}T_d : Fe^{3+}O_h$ for the magnetosomes produced in the Co(0) culture is 0.70 : 1.00 : 1.20 (this ratio is 1 : 1 : 1 for stoichiometric magnetite) (figure 3*a*,*b*). In contrast, the Co(12.1) magnetosomes are obviously non-stoichiometric with a significant decrease of the $Fe^{2+}O_h$ peak (figure 3*c*,*d*). From the linear combination, one can compute that the ratio of $(Fe^{2+} + Co^{2+})O_h : Fe^{3+}T_d : Fe^{3+}O_h$ is 0.575 : 1.00 : 1.28.

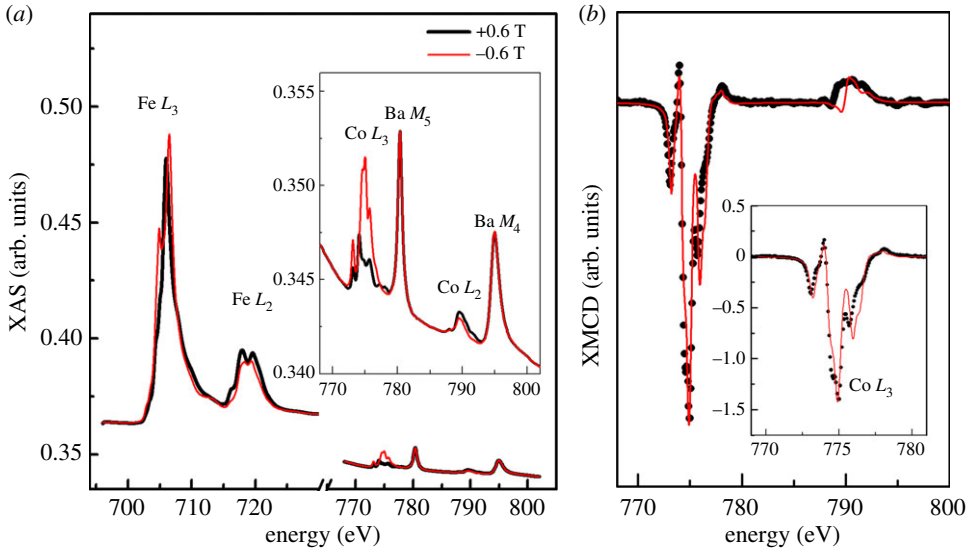

Figure 4. (*a*) Experimental XAS spectra at the Fe and Co $L_{2,3}$ edges on the Co(12.1) magnetosomes for right and left polarized X-rays in a 0.6 T magnetic field at 4 K. The baseline difference prior to the Co $L_{2,3}$ edges is due to magnetic XAFS from Fe $L_{2,3}$ edges. (*b*) Experimental XMCD signal (black dots) at the Co $L_{2,3}$ edges compared with the ligand field multiple calculated spectrum (red line) for octahedral Co^{2+} ion. The two peaks around 780 and 795 eV in (*a*) arise from the $M_{4,5}$ edges of Ba impurities in the Si wafer on which the sample was deposited (electronic supplementary material, figure S5).

Based on the previous analysis in figure 3*d*, we can estimate the difference between the experimental feature originating from Fe^{2+} and the fit that has been made. This difference can be interpreted as equal to the amount of cobalt ions that enters the magnetosomes. The cobalt concentration, defined as [Co]/([Fe] + [Co]) is found to be approximately 6% of the total metal ion content in the Co(12.1) magnetosomes. One can also determine the cobalt concentration by scaling the intensity of the XAS spectra at Co $L_{2,3}$ edges with respect to the spectra at Fe $L_{2,3}$ edges and considering the sum rule on the number of holes [39]. If the average number of holes on the Co and Fe 3d shells are considered, one finds [Co]/([Fe] + [Co]) ≈ 4% (figure 4*a*). This new result is in line with the previous value determined from the fit on the XMCD, although it is slightly less precise because of the uncertainty between the ratio of the radial integrals for the electric dipole transitions at Fe and Co $L_{2,3}$ edges. Notably, XAS and XMCD measurements were made in total electron yield mode with an effective probing depth of approximately 3–5 nm, where the signal decreases exponentially with increasing depth, hence most XAS and XMCD signal originates from the first few nanometres. Therefore, the cobalt content within magnetosomes might be overestimated in the case where the concentration of cobalt would be higher at the surface of the magnetosomes than in the bulk. To precisely determine the amounts of cobalt doping, some chemical analyses on dissolved samples of the magnetosomes are needed in the near future, e.g. the total concentration of iron can be determined by Ferrozine assay, while the relative amounts of cobalt and iron can be measured by inductively coupled plasma atomic emission spectroscopy [10,13].

The site occupancy and oxidation state of the cobalt within the magnetosomes were further studied by examining the XMCD spectra measured at the Co $L_{2,3}$ edges (figure 4*b*). Theoretical XAS and XMCD spectra have been calculated for Co^{2+} and Co^{3+} ions in both O_h and T_d coordinations (electronic supplementary material, figure S3). They have been normalized and broadened to account for instrumental broadening for comparison with the experimental spectra. The strong resemblance of the experimental data to the XAS and XMCD spectra calculated for an octahedral Co^{2+} ion suggests that the Co cations reside almost exclusively on octahedral sites (figure 4*b*). In addition, the XMCD signal at the Co L_3 edge is very large and amounts to 140% of the isotropic Co L_3 edge. This is a strong indication that the cobalt ions have to be present inside the magnetosome and cannot be paramagnetic ions polarized by neighbouring magnetite crystals, i.e. Co^{2+} ions were incorporated into the O_h sites of the spinel structure of magnetosome magnetite by substituting Fe^{2+}. This conclusion is fully in line with the observed reduced Fe^{2+} concentration in octahedral sites as concluded from the analysis of the Fe $L_{2,3}$ edge XMCD spectra.

To further evaluate the Co^{2+} substitution and its effect on the magnetic properties of the magnetosomes, we have measured element-specific magnetization curves detected by XMCD at the Fe and Co $L_{2,3}$ edges at approximately 3 K. From figure 5, it is possible to gain information on the repartition of cobalt ions inside the magnetosomes. One first finds that the coercivity measured at the Fe $L_{2,3}$ edges is 9 times larger for the Co(12.1) magnetosomes, approximately 210 mT (figure 5*b*), than for the Co(0) magnetosomes, approximately 23 mT (figure 5*a*). This is a very strong confirmation that cobalt ions are incorporated inside the spinel structure of magnetosomes and increase the coercivity of the whole magnetite crystals. One also observes that for the Co(12.1) magnetosomes the magnetization curves measured at Co and Fe $L_{2,3}$ edges are slightly different (figure 5*b*). One notes that the normalized remanent magnetization (i.e. remanent magnetization divided by magnetization at saturation) for the magnetization curve measured at Co $L_{2,3}$ edges is 89%, whereas it is 82% for the curve measured at the Fe $L_{2,3}$ edges. In contrast, the remanent magnetization for the Co(0) magnetosomes is equal to 33% of the magnetization at saturation. A simple rule of proportionality then indicates that around 90% of the magnetosomes have incorporated cobalt ions, whereas 10% have not and remained pure Fe bearing magnetites. From these determinations, one can compute the expected magnetization curve and coercivity using the magnetization curve measured on the Co(0) magnetosomes at the Fe $L_{2,3}$ edges and on the Co(12.1) magnetosomes

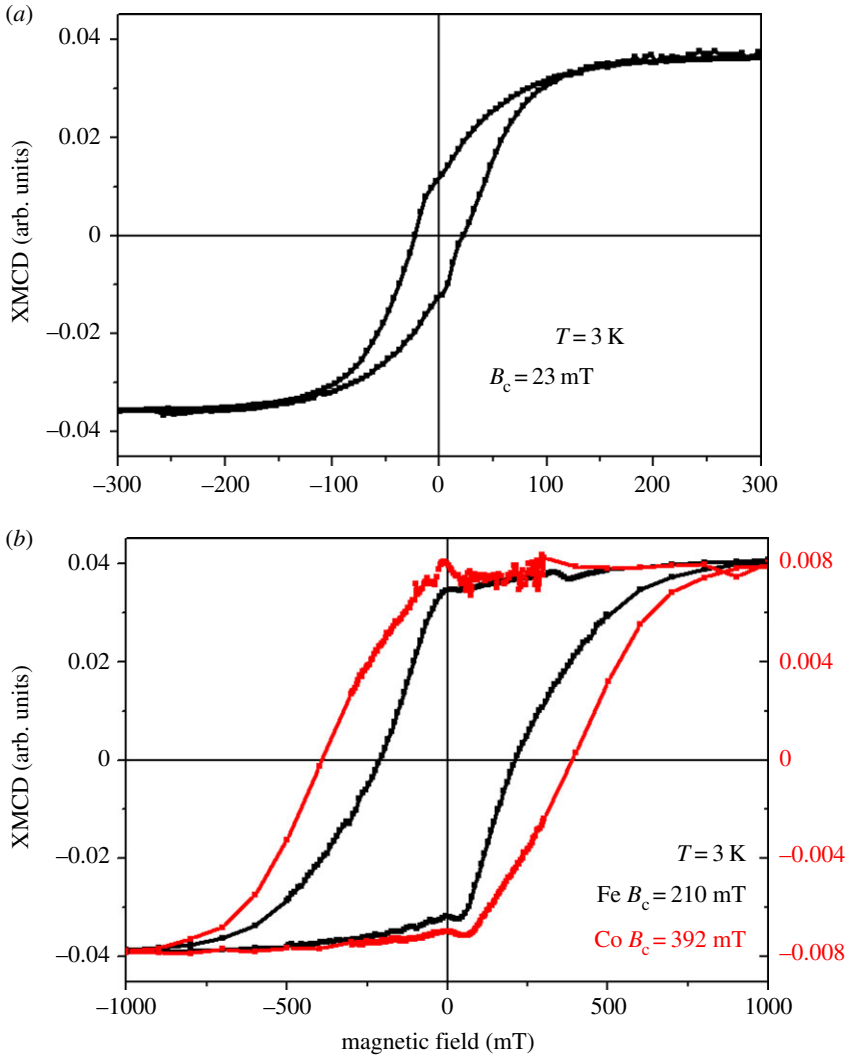

Figure 5. Element-specific magnetization curves detected at 3 K by XMCD at the Fe (black line) and Co (red line) L_3 edges in the Co(0) magnetosomes (*a*) and Co(12.1) magnetosomes (*b*). Note that the *x*-axis is different for the two types of magnetosomes.

at the Co $L_{2,3}$ edges (electronic supplementary material, figure S4). A straightforward comparison indicates that the linear combination is quite different from what has been actually measured on the Co(12.1) magnetosomes at the Fe $L_{2,3}$ edges. We interpret this difference as a sign that Co is not homogeneously distributed inside the magnetosomes. In this picture, we expect a gradient of cobalt concentration with the largest concentration at the surface of the magnetosomes. The magneto-crystalline anisotropy of cobalt ions combined with the surface anisotropy would tend to increase the coercivity values. For Fe, the surface anisotropy would not contribute as much because of its distribution inside the whole bulk of the magnetosome. This scenario also explains the lower coercivity for Fe than for cobalt in the Co(12.1) magnetosomes.

4. Discussion and conclusion

The chemical purity of magnetite produced by MTB has been discussed for many years. On the one hand, the magnetosome formation is genetically controlled, resulting in a well-ordered crystal structure, nearly perfect stoichiometry and narrow size distribution, thus well-defined magnetic properties [24,25]. Such crystallographic, magnetic and chemical properties have been widely used as potential criteria for identifying fossils of magnetosomes (i.e. magnetofossils) from ancient sediments or rocks [26,45]. On the other hand, to tune their magnetism suitable for various applications, great efforts have been made over the last decade in incorporating other transition metals such as Co, Mn, Zn, Cu and Ni into magnetosomes [11,13,14]. Very recently, Amor *et al*. [46] tested the incorporation of 34 trace elements including some transition, light and heavy metals in magnetosomes produced by *M. magneticum* AMB-1. They found that, despite very low concentration (approx. 1–10 ppm), most trace elements within the magnetosomes can be measurable by high-resolution inductively coupled plasma mass spectrometry. In the present study, we have investigated for the first time the coordination chemistry and magnetism of cobalt-doped magnetosomes with XMCD for element- and site-specific magnetic analysis. Experimental and theoretical XMCD analyses at both Fe and Co $L_{2,3}$ edges demonstrate unambiguously that Co^{2+} was incorporated within the spinel structure of magnetosomes by the substitution of Fe^{2+} at the O_h sites. Such substitution may occur heterogeneously, e.g. a gradient of cobalt concentration with the largest concentration at the surface of the magnetosomes, resulting in a joint effect of magneto-crystalline anisotropy of cobalt ions and surface anisotropy on increasing the coercivity of cobalt-doped particles. We further studied the cobalt distribution among different particles with EDXS in TEM mode. The results clearly show that the cobalt concentration varies from particle to particle even within the same

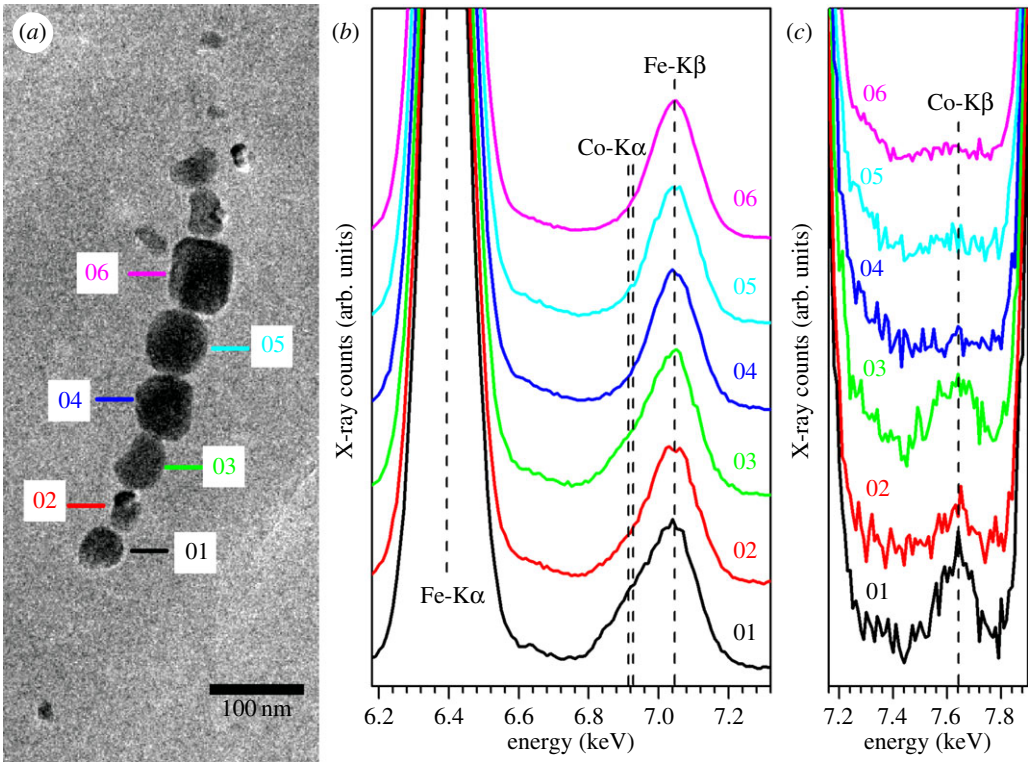

Figure 6. EDXS measurements performed on individual magnetosome particles. (*a*) TEM image of one magnetosome chain within one same cell which was analysed by EDXS in TEM mode. (*b,c*) EDX spectra of six individual particles as indicated by the numbers in (*a*). For each particle, the EDX spectrum was recorded with a counting time of 4 min and an electron probe of several nanometres to optimize a good signal to noise ratio and to minimize the induced irradiation damage of the particles. All the EDX spectra were normalized by their own Fe-Kα peak, and therefore the degree of asymmetry of Fe-Kβ peak (approx. 7.05 keV) and the intensity of Co-Kβ peak (approx. 6.92 keV) could be compared among the six individual particles and closely related to their cobalt amounts. Clearly, those cobalt-doped magnetosomes are characterized by an obviously asymmetric Fe-Kβ peak (approx. 7.05 keV) with a small shoulder at approximately 6.92 keV (i.e. Co-Kα peak) along with a small Co-Kβ peak at approximately 7.65 keV, i.e. particles 1–3 may contain more cobalt than particles 4–6.

magnetosome chain within the same cell (figure 6). Those cobalt-doped magnetosomes are characterized by an obviously asymmetric Fe-Kβ peak (approx. 7.05 keV) with a small shoulder at approximately 6.92 keV (i.e. Co-Kα peak) along with a small Co-Kβ peak at approximately 7.65 keV (e.g. particles 1–3 in figure 6). These new results, consistent with the bulk magnetic properties (e.g. reduced T_v and wasp-waisted hysteresis loop) and element- and site-specific XMCD results, altogether demonstrate that some magnetosomes within AMB-1 present a heterogeneous doping by Co^{2+} in the octahedral sites of magnetite.

Partially consistent with previous observation of a toxic effect of cobalt on AMB-1 cell growth [11], the present study shows that the addition of 12.1 µM of Co^{2+} in the initial culture medium significantly delays the cell growth and slightly decreases the final cell density compared with the Co(2.1) culture which contains a trace amount of cobalt (2.1 µM) (electronic supplementary material, figure S6). Importantly, this study reveals that, compared with the Co(0) culture, i.e. without any cobalt in the initial growth medium, the presence of trace cobalt can significantly improve the magnetosome formation and the cell growth in the Co(2.1) culture, i.e. more magnetosomes with larger sizes and longer chains (figure 1), and higher final cell density in the latter than the former (electronic supplementary material, figure S6). This indicates that trace cobalt benefits the cell growth and magnetosome formation within AMB-1. Actually, cobalt is a bio-essential metal for life, either forming the central cobalt–corrin complex of cobalamin (vitamin B12) or directly binding in enzymes such as nitrile hydratase and carbonic anhydrase [47]. We assume that cobalt is necessary for biosynthesis of B12 or some key enzymes which might be linked to magnetosome formation within AMB-1. An active or/and passive transport of excess cobalt to cells or cell walls (periplasm) may occur when AMB-1 is growing in cobalt-containing medium. Cobalt ions may compete with iron ions for sites of cation diffusion system on the magnetosome membrane, and then it is co-transported into the magnetosome membrane and co-precipitated as cobalt-doped magnetite. Alternatively, within the periplasm, cobalt ions can be initially co-precipitated within ferrihydrite, precursor for magnetosome magnetite [48], and further form cobalt-doped magnetite by recrystallization reaction within magnetosome membrane. A heterogeneous distribution of cobalt within inter- and inner-magnetosomes suggests that Co^{2+} might be largely incorporated in magnetosomes only when Fe^{3+} in the medium is largely consumed for building magnetite. Within the whole-genomic information on AMB-1, an ECF-type Co^{2+} transporter gene cluster CbiMNQO (Amb0275–Amb0278), a cobalamin synthesis gene cluster (Amb0292–Amb0298), and a cobalt–precorrin synthesis gene cluster (Amb2641 and Amb2642) were found and presumed to be the respective homologous genes [49]. The roles of these genes in the transport and incorporation of cobalt into magnetosomes would deserve further studies.

Cobalt doping in magnetite nanoparticles has also been performed in Fe^{3+}-reducing bacteria which produce large quantities of superparamagnetic magnetite extracellularly [10,12]. Compared with trace cobalt (approx. 1–3%) doping in magnetosome magnetite in previous studies [11,13] and approximately 4–6% in the present one, the amounts of cobalt doped in extracellular magnetite can be much larger, e.g. the atom ratio of Co/Fe can reach up to approximately

50% [10,12]. Besides the presence of Co^{2+} ions in the O_h sites, up to 17% Co^{2+} ions can also be incorporated into T_d sites [10]. From an application point of view, a precise doping by which the valence, site occupancy and content of cobalt in the spinel structure of magnetite can be controlled is crucial for producing promising MNPs with precisely controlled magnetic properties. To use cobalt-doped magnetosomes for cancer therapy for instance [29], chains of magnetosomes doped with suitable amounts of cobalt have higher efficiency compared with other MNPs due to a good compromise between coercivity increasing and magnetization decreasing [50]. This study demonstrates that cobalt can be exclusively incorporated into the spinel structure of magnetosome magnetite at the O_h sites as Co^{2+} which significantly increases the coercivity at both ambient and low temperatures. Consistent with previous studies [13,25,30,46], this study further demonstrates that the biomineralization process of magnetosomes within MTB system could be affected by environmental factors such as medium components. While MTB do biomineralize in a very ordered, precise manner to form chain-arranged SD magnetites with narrow size and shape distributions, the chemical and therefore magnetic properties of magnetosomes can be tuned by an incorporation of Co^{2+} into O_h sites of magnetites through the replacement of Fe^{2+} ions. Since significant progress has been achieved recently in the large-scale production of magnetosomes [51] and the biosynthesis in a foreign microorganism by transfer of magnetosome gene clusters [52], MTB may provide a promising biomimetic system for precisely producing chains of Co^{2+}-doped SD magnetite which have optimizing magnetic properties, i.e. enhanced coercivity but not-too-low saturation magnetization, as well as uniaxial in-plane anisotropy.

In conclusion, we carried out a systematic study on the cobalt doping in magnetosome magnetite within *M. magneticum* AMB-1 by the combination of (S)TEM, bulk magnetic measurements, and element- and site-specific XMCD analyses. All data are consistent and clearly reveal that (i) trace amount of cobalt within the initial growth medium (i.e. 2.1 μM) can significantly improve both the cell growth and magnetosome formation; (ii) Co^{2+} ions can be exclusively incorporated into O_h sites of magnetosome magnetite through the replacement of Fe^{2+} ions; (iii) Co^{2+} ions occur in the spinel structure of magnetosomes heterogeneously, i.e. they vary in the amount of different particles and enrich at the surface of individual ones; and (iv) the controlled doping of Co^{2+} in O_h sites of magnetosome magnetite resulted in a pronounced increase in magneto-crystalline anisotropy and magnetic coercivity.

Authors' contributions. J.H.L., N.M., P.S. and Y.X.P. designed research. J.H.L., Y.Z.W. and H.T.C. cultured bacteria, prepared samples and performed rock magnetic measurements. J.H.L. and N.M. performed (S)TEM observations. P.S., N.M., A.J., M.A., J.H.L., O.B., E.O. and P.O. performed XAS and XMCD experiments and processed data. J.H.L., P.S., N.M., M.A., A.J. and Y.X.P. wrote the paper. All authors discussed results and commented on the manuscript.

Competing interests. We declare we have no competing interests.

Funding. This study was financially supported by the National Natural Science Foundation of China (grant nos. 41374004, 41522402 and 41330104) and the French programme ANR-blanc (project MS-MCNP and project SWITCH). J.H.L. benefits from the Open Project Support from the State Key Laboratory of Lithospheric Evolution (SKLLE, Beijing).

Acknowledgements. We thank Prof. Wu Long-Fei and Dr Yohan Guyodo for useful discussions. We are also grateful to the SOLEIL staff for smoothly running the facility. J.H.L. benefits from the discussions in Coffice 442 of the Institute of Geology and Geophysics, Chinese Academy of Sciences (IGGCAS).

References

1. Reiss G, Hutten A. 2005 Magnetic nanoparticles: applications beyond data storage. *Nat. Mater*. **4**, 725–726. (doi:10.1038/Nmat1494)
2. Guardia P, Di Corato R, Lartigue L, Wilhelm C, Espinosa A, Garcia-Hernandez M, Gazeau F, Manna L, Pellegrino T. 2012 Water-soluble iron oxide nanocubes with high values of specific absorption rate for cancer cell hyperthermia treatment. *ACS Nano* **6**, 3080–3091. (doi:10.1021/nn2048137)
3. Martin M, Carmona F, Cuesta R, Rondon D, Galvez N, Dominguez-Vera JM. 2014 Artificial magnetic bacteria: living magnets at room temperature. *Adv. Funct. Mater*. **24**, 3489–3493. (doi:10.1002/adfm.201303754)
4. Sun S. 2006 Recent advances in chemical synthesis, self-assembly, and applications of FePt nanoparticles. *Adv. Mater*. **18**, 393–403. (doi:10.1002/adma.200501464)
5. Alphandéry E, Faure S, Seksek O, Guyot F, Chebbi I. 2011 Chains of magnetosomes extracted from AMB-1 magnetotactic bacteria for application in alternative magnetic field cancer therapy. *ACS Nano* **5**, 6279–6296. (doi:10.1021/nn201290k)
6. Li JH, Ge KP, Pan YX, Williams W, Liu QS, Qin HF. 2013 A strong angular dependence of magnetic properties of magnetosome chains: implications for rock magnetism and paleomagnetism. *Geochem. Geophys. Geosyst*. **14**, 3887–3907. (doi:10.1002/Ggge.20228)
7. Alphandéry E, Ding Y, Ngo AT, Wang ZL, Wu LF, Pileni MP. 2009 Assemblies of aligned magnetotactic bacteria and extracted magnetosomes: what is the main factor responsible for the magnetic anisotropy? *ACS Nano* **3**, 1539–1547. (doi:10.1021/nn900289n)
8. Körnig A, Winklhofer M, Baumgartner J, Gonzalez TP, Fratzl P, Faivre D. 2014 Magnetite crystal orientation in magnetosome chains. *Adv. Funct. Mater*. **24**, 3926–3932. (doi:10.1002/adfm.201303737)
9. Sun S-N, Wei C, Zhu Z-Z, Hou Y-L, Venkatraman SS, Xu Z-C. 2014 Magnetic iron oxide nanoparticles synthesis and surface coating techniques for biomedical applications. *Chin. Phys. B* **23**, 037503. (doi:10.1088/1674-1056/23/3/037503)
10. Byrne JM *et al.* 2013 Controlled cobalt doping in biogenic magnetite nanoparticles. *J. R. Soc. Interface* **10**, 20130134. (doi:10.1098/rsif.2013.0134)
11. Tanaka M, Brown R, Hondow N, Arakaki A, Matsunaga T, Staniland S. 2012 Highest levels of Cu, Mn and Co doped into nanomagnetic magnetosomes through optimized biomineralisation. *J. Mater. Chem*. **22**, 11 919–11 921. (doi:10.1039/C2jm31520c)
12. Coker VS, Telling ND, van der Laan G, Pattrick RAD, Pearce CI, Arenholz E, Tuna F, Winpenny REP, Lloyd JR. 2009 Harnessing the extracellular bacterial production of nanoscale cobalt ferrite with exploitable magnetic properties. *ACS Nano* **3**, 1922–1928. (doi:10.1021/nn900293d)
13. Staniland S, Williams W, Telling N, Van Der Laan G, Harrison A, Ward B. 2008 Controlled cobalt doping of magnetosomes *in vivo*. *Nat. Nanotechnol*. **3**, 158–162. (doi:10.1038/nnano.2008.35)
14. Prozorov T *et al.* 2014 Manganese incorporation into the magnetosome magnetite: magnetic signature of doping. *Eur. J. Mineral*. **26**, 457–471. (doi:10.1127/0935-1221/2014/0026-2388)
15. Byrne JM *et al.* 2014 Biosynthesis of zinc substituted magnetite nanoparticles with enhanced magnetic properties. *Adv. Funct. Mater*. **24**, 2518–2529. (doi:10.1002/adfm.201303230)
16. Coker VS *et al.* 2010 Microbial engineering of nanoheterostructures: biological synthesis of a magnetically recoverable palladium nanocatalyst. *ACS Nano* **4**, 2577–2584. (doi:10.1021/nn9017944)
17. Wang L, Prozorov T, Palo PE, Liu X, Vaknin D, Prozorov R, Mallapragada S, Nilsen-Hamilton M. 2012 Self-

assembly and biphasic iron-binding characteristics of Mms6, a bacterial protein that promotes the formation of superparamagnetic magnetite nanoparticles of uniform size and shape. *Biomacromolecules* **13**, 98–105. (doi:10.1021/bm201278u)

18. Prozorov T *et al.* 2007 Protein-mediated synthesis of uniform superparamagnetic magnetite nanocrystals. *Adv. Funct. Mater.* **17**, 951–957. (doi:10.1002/adfm.200600448)
19. Bird SM, Rawlings AE, Galloway JM, Staniland SS. 2016 Using a biomimetic membrane surface experiment to investigate the activity of the magnetite biomineralisation protein Mms6. *RSC Advances* **6**, 7356–7363. (doi:10.1039/C5RA16469A)
20. Rawlings AE, Bramble JP, Walker R, Bain J, Galloway JM, Staniland SS. 2014 Self-assembled MmsF proteinosomes control magnetite nanoparticle formation *in vitro*. *Proc. Natl Acad. Sci. USA* **111**, 16 094–16 099. (doi:10.1073/pnas.1409256111)
21. Galloway JM, Staniland SS. 2012 Protein and peptide biotemplated metal and metal oxide nanoparticles and their patterning onto surfaces. *J. Mater. Chem.* **22**, 12 423–12 434. (doi:10.1039/C2jm31620j)
22. Galloway JM, Bramble JP, Rawlings AE, Burnell G, Evans SD, Staniland SS. 2012 Nanomagnetic arrays formed with the biomineralization protein Mms6. *J. Nano Res.* **17**, 127–146. (doi:10.4028/www.scientific.net/JNanoR.17.127)
23. Galloway JM, Arakaki A, Masuda F, Tanaka T, Matsunaga T, Staniland SS. 2011 Magnetic bacterial protein Mms6 controls morphology, crystallinity and magnetism of cobalt-doped magnetite nanoparticles *in vitro*. *J. Mater. Chem.* **21**, 15 244–15 254. (doi:10.1039/C1jm12003d)
24. Bazylinski DA, Frankel RB. 2004 Magnetosome formation in prokaryotes. *Nat. Rev. Microbiol.* **2**, 217–230. (doi:10.1038/nrmicro842)
25. Faivre D, Schüler D. 2008 Magnetotactic bacteria and magnetosomes. *Chem. Rev.* **108**, 4875–4898. (doi:10.1021/cr078258w)
26. Li JH, Benzerara K, Bernard S, Beyssac O. 2013 The link between biomineralization and fossilization of bacteria: insights from field and experimental studies. *Chem. Geol.* **359**, 49–69. (doi:10.1016/j.chemgeo.2013.09.013)
27. Prozorov T, Bazylinski DA, Mallapragada SK, Prozorov R. 2013 Novel magnetic nanomaterials inspired by magnetotactic bacteria: topical review. *Mater. Sci. Eng. R* **74**, 133–172. (doi:10.1016/j.mser.2013.04.002)
28. Taherkhani S, Mohammadi M, Daoud J, Martel S, Tabrizian M. 2014 Covalent binding of nanoliposomes to the surface of magnetotactic bacteria for the synthesis of self-propelled therapeutic agents. *ACS Nano* **8**, 5049–5060. (doi:10.1021/nn5011304)
29. Alphandéry E, Carvallo C, Menguy N, Chebbi I. 2011 Chains of cobalt doped magnetosomes extracted from AMB-1 magnetotactic bacteria for application in alternative magnetic field cancer therapy. *J. Phys. Chem. C* **115**, 11 920–11 924. (doi:10.1021/jp201274g)
30. Li JH, Pan YX. 2012 Environmental factors affect magnetite magnetosome synthesis in *Magnetospirillum magneticum* AMB-1: implications for biologically controlled mineralization. *Geomicrobiol. J.* **29**, 362–373. (doi:10.1080/01490451.2011.565401)
31. Li JH, Wu WF, Liu QS, Pan YX. 2012 Magnetic anisotropy, magnetostatic interactions and identification of magnetofossils. *Geochem. Geophys. Geosyst.* **13**, Q10Z51. (doi:10.1029/2012gc004384)
32. Friedrich H, McCartney MR, Buseck PR. 2005 Comparison of intensity distributions in tomograms from BF TEM, ADF STEM, HAADF STEM, and calculated tilt series. *Ultramicroscopy* **106**, 18–27. (doi:10.1016/j.ultramic.2005.06.005)
33. Roberts AP, Pike CR, Verosub KL. 2000 First-order reversal curve diagrams: a new tool for characterizing the magnetic properties of natural samples. *J. Geophys. Res.* **105**, 28 461–28 475. (doi:10.1029/2000JB900326)
34. Harrison RJ, Feinberg JM. 2008 FORCinel: an improved algorithm for calculating first-order reversal curve distributions using locally weighted regression smoothing. *Geochem. Geophys. Geosyst.* **9**, Q05016. (doi:10.1029/2008GC001987)
35. Moskowitz BM, Frankel RB, Bazylinski DA. 1993 Rock magnetic criteria for the detection of biogenic magnetite. *Earth Planet. Sci. Lett.* **120**, 283–300. (doi:10.1016/0012-821X(93)90245-5)
36. Ohresser P *et al.* 2014 DEIMOS: a beamline dedicated to dichroism measurements in the 350–2500 eV energy range. *Rev. Sci. Instrum.* **85**, 013106. (doi:10.1063/1.4861191)
37. Guyodo Y *et al.* 2012 X-ray magnetic circular dichroïsm provides strong evidence for tetrahedral iron in ferrihydrite. *Geochem. Geophys. Geosyst.* **13**, Q06Z44. (doi:10.1029/2012GC004182)
38. Carvallo C, Sainctavit P, Arrio M-A, Menguy N, Wang Y, Ona-Nguema G, Brice-Profeta S. 2008 Biogenic vs. abiogenic magnetite nanoparticles: a XMCD study. *Am. Mineral.* **93**, 880–885. (doi:10.2138/am.2008.2713)
39. Thole BT, Vanderlaan G, Fabrizio M. 1994 Magnetic ground-state properties and spectral distributions. I. X-ray-absorption spectra. *Phys. Rev. B* **50**, 11 466–11 473. (doi:10.1103/PhysRevB.50.11466)
40. Arrio MA, Sainctavit P, Cartier dit Moulin C, Mallah T, Verdaguer M, Pellegrin E, Chen CT. 1996 Characterization of chemical bonds in bimetallic cyanides using X-ray absorption spectroscopy at $L_{2,3}$ edges. *J. Am. Chem. Soc.* **118**, 6422–6427. (doi:10.1021/ja9542698)
41. Li JH, Pan YX, Chen GJ, Liu QS, Tian LX, Lin W. 2009 Magnetite magnetosome and fragmental chain formation of *Magnetospirillum magneticum* AMB-1: transmission electron microscopy and magnetic observations. *Geophys. J. Int.* **177**, 33–42. (doi:10.1111/j.1365-246X.2009.04043.x)
42. Walz F. 2002 The Verwey transition: a topical review. *J. Phys.* **14**, R285. (doi:10.1088/0953-8984/14/12/203)
43. Dunlop DJ, Özdemir Ö. 1997 *Rock magnetism: fundamentals and frontiers*. London, UK: Cambridge University Press.
44. Tauxe L, Mullender TAT, Pick T. 1996 Potbellies, wasp-waists, and superparamagnetism in magnetic hysteresis. *J. Geophys. Res.* **101**, 571–583. (doi:10.1029/95JB03041)
45. Kopp RE, Kirschvink JL. 2008 The identification and biogeochemical interpretation of fossil magnetotactic bacteria. *Earth-Sci. Rev.* **86**, 42–61. (doi:10.1016/j.earscirev.2007.08.001)
46. Amor M *et al.* 2015 Chemical signature of magnetotactic bacteria. *Proc. Natl Acad. Sci. USA* **112**, 1699–1703. (doi:10.1073/pnas.1414112112)
47. Banerjee R, Ragsdale SW. 2003 The many faces of Vitamin B12: catalysis by cobalamin-dependent enzymes. *Annu. Rev. Biochem.* **72**, 209–247. (doi:10.1146/annurev.biochem.72.121801.161828)
48. Faivre D, Böttger LH, Matzanke BF, Schüler D. 2007 Intracellular magnetite biomineralization in bacteria proceeds by a distinct pathway involving membrane-bound ferritin and an iron(II) species. *Angew. Chem. Int. Ed. Engl.* **46**, 8495–8499. (doi:10.1002/anie.200700927)
49. Matsunaga T, Okamura Y, Fukuda Y, Wahyudi AT, Murase Y, Takeyama H. 2005 Complete genome sequence of the facultative anaerobic magnetotactic bacterium *Magnetospirillum* sp. strain AMB-1. *DNA Res.* **12**, 157–166. (doi:10.1093/dnares/dsi002)
50. Obaidat IM, Issa B, Haik Y. 2015 Magnetic properties of magnetic nanoparticles for efficient hyperthermia. *Nanomaterials* **5**, 63–89. (doi:10.3390/nano5010063)
51. Liu Y, Li GR, Guo FF, Jiang W, Li Y, Li LJ. 2010 Large-scale production of magnetosomes by chemostat culture of *Magnetospirillum gryphiswaldense* at high cell density. *Microb. Cell Fact.* **9**, 99. (doi:10.1186/1475-2859-9-99)
52. Kolinko I *et al.* 2014 Biosynthesis of magnetic nanostructures in a foreign organism by transfer of bacterial magnetosome gene clusters. *Nat. Nanotechnol.* **9**, 193–197. (doi:10.1038/nnano.2014.13)